ISSN 2347 - 3983
Volume 14. No.6, June 2026
International Journal of Emerging Trends in Engineering Research
Available Online at http://www.warse.org/IJETER/static/pdf/file/ijeter0114062026.pdf
https://doi.org/10.30534/ijeter/2026/0114062026

Electric Stress Analysis of Ageing 400 KV Composite Insulator Profiles Having Internal Defects

Vrushank S. Chavan[1], Hiren M. Patel[2], Dr. Anil S. Khopkar[3]
[1]The Maharaja Sayajirao University of Baroda, India, vrushank.msu@gmail.com
[2]The Maharaja Sayajirao University of Baroda, India, hiren.m.patel-eed@msubaroda.ac.in
[3]Electrical Research and Development Association, India, research.electrical@rediffmail.com

Received Date: May 1, 2026 Accepted Date: June 2, 2026 Published Date: June 07, 2026

ABSTRACT

Ageing insulators develop internal defects such as moisture ingress or voids within the FRP rod of composite insulators which are difficult to detect and can accelerate degradation. Electric stress analysis had been reported for such insulator defects, but the influence of shed profile which usually is optimized for creepage and pollution performance on internal defect behavior remains largely unexplored. This study examines whether shed profile geometry affects internal defect severity for insulators of the same voltage class. A comparative 2D FEM model was developed in COMSOL for two 400 kV composite insulator profiles, differing only in shed geometry, under identical defect conditions. Results show defect position and length consistently govern the type and severity of field distortion in both profiles, while shed profile systematically alters the magnitude and symmetry of the electric stress. This confirms a measurable interaction between internal defect behavior and shed geometry, relevant to insulator design and diagnostic strategy.

Key words: Composite insulator, Ageing, Shed profile, Internal defect, Finite element analysis (FEM).

1. INTRODUCTION

Electrical insulators isolate energized conductors from grounded supports while bearing the line's mechanical load. Porcelain and glass long dominated this role but were prone to pollution flashover due to weight, brittleness, and hydrophilic surfaces. This brought the shift from the 1970s onward to composite insulators, using an FRP rod core for mechanical support and a silicone rubber or EPDM housing for weathering and electrical protection, offering better pollution performance and lower weight [1], [2].

However, insulator reliability depends heavily on the internal FRP rod, which can develop conductive imperfections through manufacturing defects (unfilled resin channels drawing moisture) or service induced discharge causing localized carbonization [2],[3]. Field studies confirm such internal defects distort the axial electric field, with defect location and size identifiable by comparing field profiles against an intact rod, and the resulting field concentration at defect edges can trigger further discharge, compounding the defect over time [4],[5]. This cavity field distortion mechanism has also been verified at full operating scale, where manufacturing origin cavities in EHV insulator housings distorted local fields and initiated discharge, confirming the mechanism is general rather than lab specific [6].

Abnormal heating at the high voltage end of composite insulators arises primarily from dielectric degradation of the silicone rubber sheath, not surface contamination. Moisture absorption from sheath aging increases the dielectric constant and loss factor, inducing electric field distortion at the shed root [7]. 3D FEM simulation of internal semi conductive defects (varying length/position) showed the radial E-field component is consistently more sensitive to defects than the axial one, with distortion increasing with defect length. Maximum distortion occurs near defect extremities, serving as a reliable detection signature, while insulator length and grading rings showed no significant effect [8]. 3D FEM modeling of internal defects in a 28 kV insulator showed distortion was significantly larger at the shank surface than the shed extremity, with the radial component more affected there. Floating potential defects were undetectable at the shed extremity but clearly visible at the shank surface, highlighting that measurement proximity governs detection sensitivity [9]. Electro-optic measurements and 3D BEM simulations showed defects connected to the HV electrode produced the largest field distortion, while grounded electrode defects caused negligible change. Field distortion decreased sharply with radial distance, and low conductivity defects produced minimal change compared to highly conductive ones [10]. This IEEE Task Force overview identifies insulator geometry, end fitting design, and corona ring configuration as key factors governing E-field distribution, with magnitudes highest near the energized end. It confirms end fitting geometry and shed profile directly reshape field distribution and provides benchmark critical E-field values [11]. FEM modeling of a 500 kV insulator showed the defect free field profile is smooth and U-shaped, while conductive defects sharply raise the field at the high voltage end as defect length increases. Distortion intensifies as the defect moves closer to the high voltage end [12]. 3D FEM simulation on a 10 kV insulator showed sheath damage and internal defects caused sharp local field distortion at the fault site, with the radial component more sensitive than the axial one. Surface fouling behaved oppositely, reducing the axial field while increasing the radial field at both ends [13]. Experimental analysis of field aged insulators showed chemical degradation, surface roughening, and reduced hydrophobicity/tensile strength near the high voltage end. FEM simulation confirmed field enhancement concentrates at the triple junction, and FGM layers with tuned switching thresholds substantially reduce this concentration [14].

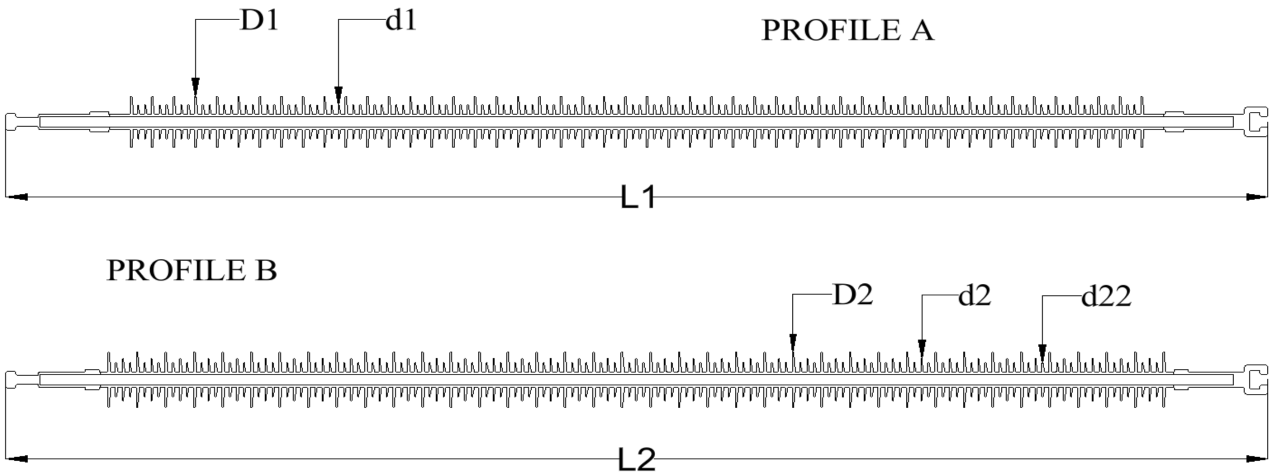

Figure 1: 2D model of 400KV Insulator Profiles

Prior work has shown that conductive defects in the FRP rod distort the surrounding electric field depending on their length and position, but this has always been studied on a single, fixed insulator shed profile. The insulator's external geometry, a parameter independently chosen by utilities for a given voltage class has not itself been examined as a variable influencing this defect induced stress distribution. This raises the question, does profile design alter how a given internal defect influence electric stress, for insulators of the same voltage class? This paper addresses that question through a comparative finite element analysis of two insulator profiles under identical defect conditions.

2. INSULATORS MODELLING AND NUMERICAL ANALYSIS

2.1 Geometrical Model of 400KV Insulator Profiles

Two 400 kV class composite insulator profiles were modeled, both sharing an identical overall insulator length, Ball and Socket ends and FRP core rod diameter, so that shed geometry remains the sole independent variable between the two configurations. A shown in figure 1, profile A employs a simpler repeating unit of one large shed followed by two smaller sheds before the next large shed. The large shed diameter is D1, and the two intermediate sheds share a single diameter d1. This profile has shorter creepage length compared to Profile B. Profile B employs a repeating unit of one large shed followed by three smaller sheds before the next large shed. The large shed diameter is D2, while the three intermediate sheds alternate between two diameters, d2 and d22. This configuration maximizes its creepage length. Both insulator profiles have same FRP rod diameter of 24 mm. The detail dimensions are mentioned in table 1.

Table 1: Technical Specifications of Insulator Profiles

Parameter	Symbol	Profile A	Profile B
Voltage Ratings	Volts	400KV	400KV
Overall insulator length	L1/L2	2700 mm	2700 mm
Large shed diameter	D1/D2	120 mm	130 mm
Small shed diameter	d1/d2	80 mm	100 mm
Small shed diameter	d22	-	80 mm
No. of large sheds	N1/N2	48	38
No. of small sheds	n1/n2	94	111
Total sheds	T1/T2	142	149

2.2 Internal Defect Modeling

To study the influence of insulator shed profile on electric stress distribution, a moisture filled defect was introduced within the FRP core rod of two different defect lengths and three different axial positions, applied identically to both insulator profiles. The defect was modeled as a narrow inclusion with moisture ingress of 1 mm width and 3.5%, 20%

of the total insulator length [8],[13], positioned near the surface of the FRP rod (i.e., close to the rod housing interface). The length of short defect is 94 mm and long defect is 540 mm

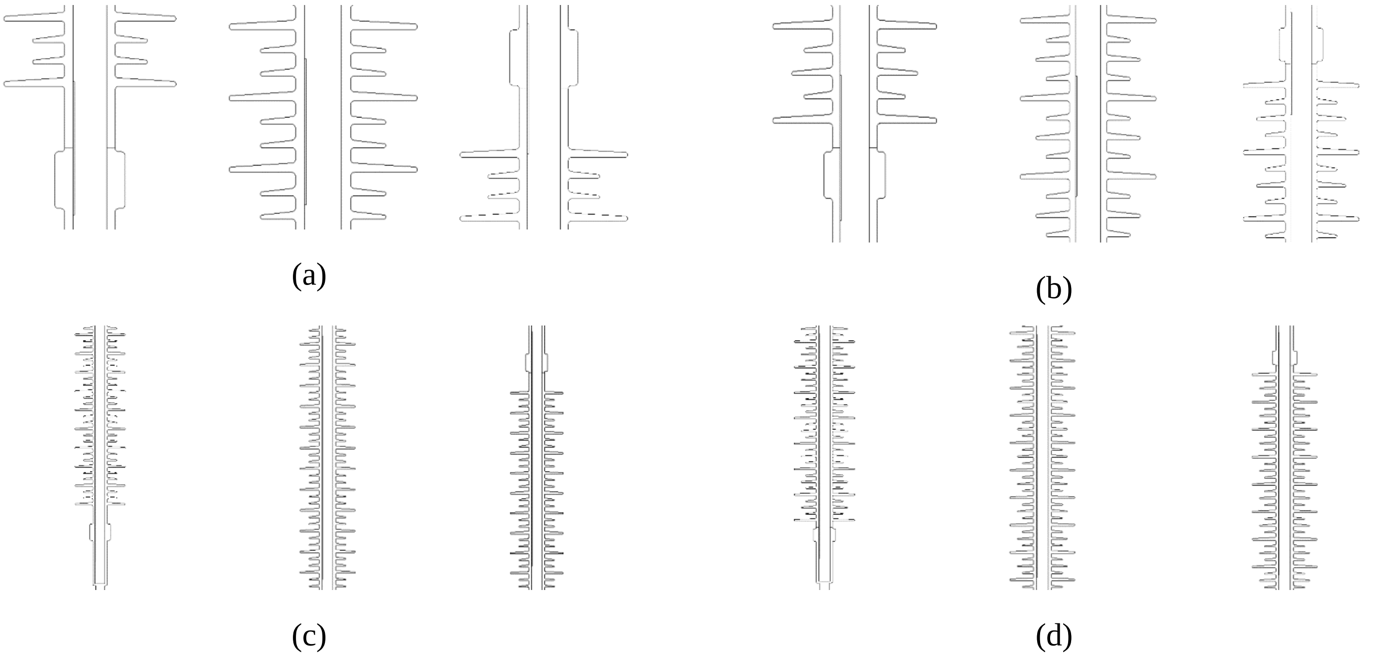

Figure 2: (a) and (b) shows the internal defect of 94 mm length while (c) and (d) shows the internal defect of 540 mm length on the profile A and B respectively.

. For each defect length, three axial positions along the FRP rod were considered at High voltage end, Center of the rod, grounded end. The combination of defect lengths, positions, for both profiles A and B are shown in Figure 2.

2.2 Finite Element Analysis

The simulation was performed in COMSOL Multiphysics using the Electrostatics interface, solved as 2D stationary studies. Each profile and configuration were built as a 2D cross section enclosed in a 10,000 mm × 10,000 mm air domain. The geometry comprised four domains air, end fittings, silicone rubber (SiR) housing, and the FRP core rod with defect cases of moisture ingress inclusion within the rod at the specified length and position. The material properties used in simulation is given in table 2. The HV end fitting was set to 326.6 kV (peak phase voltage of the 400 kV system), the grounded end to 0 V, and the outer air boundary to a zero-charge condition. A free triangular mesh "Finer" preset has been used for meshing.

The Electrostatics interface solves for the electric potential *V* based on Gauss's law, expressed in terms of the electric displacement field D:

$$\nabla D = \rho \tag{1}$$

where ρ is the space charge density. The electric displacement field is related to the electric field E as follows:

$$D = \varepsilon_0 \varepsilon_r E \tag{2}$$

where ε_0 is the permittivity of free space and ε_r is the relative permittivity of each domain given in table 2. The electric field is derived from the scalar potential *V* as:

$$E = -\nabla V \tag{3}$$

Substituting (2) and (3) into (1), and setting ρ = 0 for charge free dielectric domains, yields the governing equation solved throughout the model domain:

$$\nabla \cdot (\varepsilon_0 \varepsilon_r \nabla V) = 0 \tag{4}$$

This equation (4) is the standard form of Laplace's equation for a piecewise homogeneous dielectric medium, The electric field magnitude is computed as the norm of E, obtained directly from the gradient of the solved potential field.

Table 2: Relative permittivity of the materials

Domain	Material	εr
Air domain	Air	1
End fittings	Metal	1e10
Shed housing	SiR	4.3
Core rod	FRP	7.2
Defect	Moisture	80

3. RESULTS AND DISCUSSIONS

3.1 Electric Field and Potential Distribution of Healthy Insulator Profile

For the analysis, a junction point where the end fitting, FRP rod and SiR housing meets at both HV and LV ends are considered. Under healthy defect free conditions, as shown in Figure 3 both insulator profiles exhibit a smooth, U-shaped electric field distribution along the FRP rod, with field magnitude peaking at the high voltage (HV) end and grounded end and remaining low in the central region. Figure 4 shows the potential distribution along both insulator profiles. Table 3 compares the field norm at reference points on the HV and ground sides for both profiles.

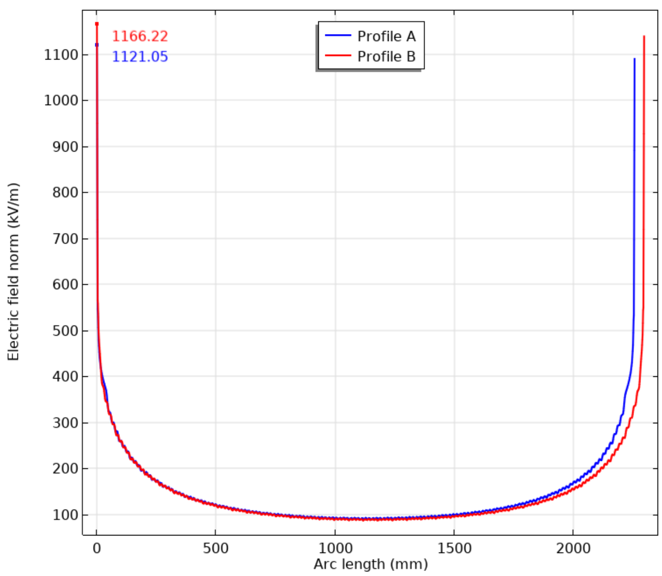

Figure 3: Electric Field Norm Along Arc Length of Healthy Insulator Profiles

Table 3: Point Evaluation of Electric Field Norm on Healthy Insulator Profiles

Electric field norm (kV/m)			
Profile A		**Profile B**	
HV side point	**LV side point**	**HV side point**	**LV side point**
638.74	619.09	663.41	644.81

Profile B shows a consistently higher field norm than Profile A at both electrodes (663.41 kV/m vs 638.74 kV/m at the HV side; 644.82 kV/m vs 619.10 kV/m at the LV side), an increase of roughly 3.9% and 4.2% respectively. Despite this baseline difference, both profiles remain well within safe operating limits for a 400 kV class insulator, confirming both designs are electrically sound in the absence of internal defects. This baseline establishes the reference against which defect induced distortion is measured.

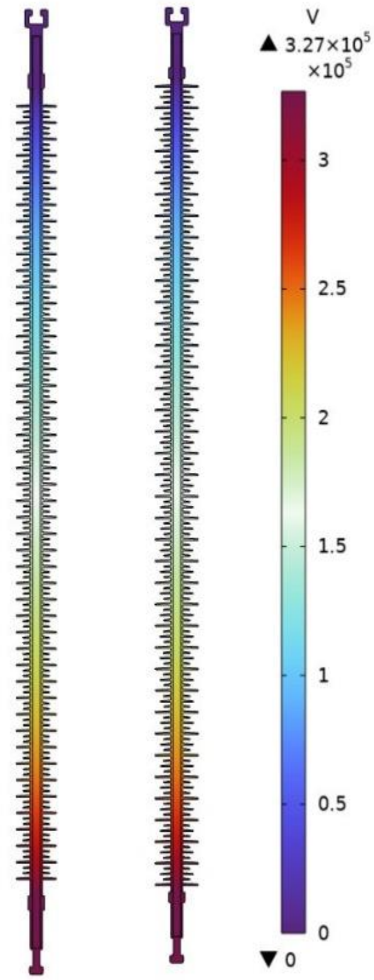

Figure 4: Electric Potential Distribution Along Insulator Profile A and Profile B Respectively

3.2 Impact of Short 94 mm Length Internal Defect on Electric Field Distribution

Introducing a 94 mm moisture defect near the surface of the FRP rod produces markedly different field responses depending on the defect's axial position, with both reference points (HV side points and LV side points, at the rod ends) and the defect's own two edges (electrode facing and rod facing) analyzed for each case. The observations of the values are presented in table 4, and the surface plot of both the profiles are given in figure 8.

For the defect at the HV side. Its electrode facing bottom edge merges electrically with the HV fitting, collapsing its own field toward zero, while the stress is transferred to the rod facing top edge 882.73 kV/m for Profile A and 1097.59 kV/m for Profile B, both well above the healthy HV side field. This redistribution is also visible at the reference points, the HV side points value drops sharply below its healthy value (profile A: 638.74 to 396.55 kV/m, −37.9%; profile B: 663.41 to 433.11 kV/m, −34.7%), while the far LV side point value is essentially unaffected (profile A: +0.3%; profile B: +0.6%). Profile B is the more severely stressed design in this configuration, showing approx. 24% higher top edge field than Profile A (1097.59 vs 882.73 kV/m) and a higher HV side point value as well. This is visible in the arc length plot figure 5 as a distinct secondary peak superimposed near the HV end of the otherwise healthy U-shaped curve, confirming the defect's disturbance is sharply localized to its own position rather than reshaping the overall field profile.

Table 4: Point Evaluation of Electric Field Norm on Insulator Profiles with 94mm defect length.

Electric field norm (kV/m)				
Defect position	**Profile A**		**Profile B**	
	HV side point	**LV side point**	**HV side point**	**LV side point**
HV side	396.55	621.06	433.10	648.97
center	635.75	621.70	666.70	646.29
Ground side	642.34	387.31	672.28	399.41
Defect position	**Bottom edge of defect**	**Top edge of defect**	**Bottom edge of defect**	**Top edge of defect**
HV side	0.06	882.73	0.06	1097.59
center	228.00	289.84	217.19	218.85
Ground side	859.44	0.061	841.90	0.06

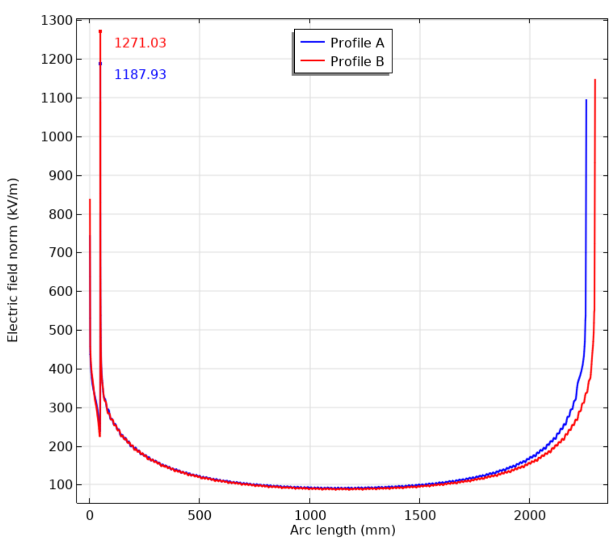

Figure 5: Electric Field Norm Along Arc Length of Insulator Profiles having 94mm defect length on HV side.

For the defect at the center, isolated from both electrodes, the defect behaves as a floating potential inclusion, and both of its edges are stressed simultaneously rather than one collapsing to zero. Reference point values stay close to healthy levels for both profiles (within ±0.6%), confirming the defect's influence stays localized. At the defect itself, however, Profile A shows a distinct asymmetry between its two edges 228.00 kV/m at the bottom and 289.85 kV/m at the top, a 27% internal difference while Profile B's two edges are nearly balanced (217.20 and 218.86 kV/m, <1% difference). The arc length plot figure 6 shows this as a narrow double spike near the mid span arc length corresponding to the defect's two edges, with the curve returning to the healthy baseline (~90–100 kV/m) almost immediately on either side visually confirming the defect's effect does not propagate along the rod.

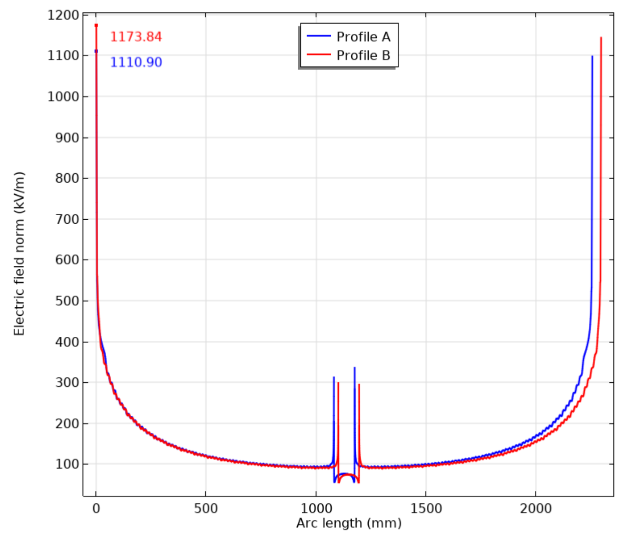

Figure 6: Electric Field Norm Along Arc Length of Insulator Profiles having 94mm defect length at floating potential

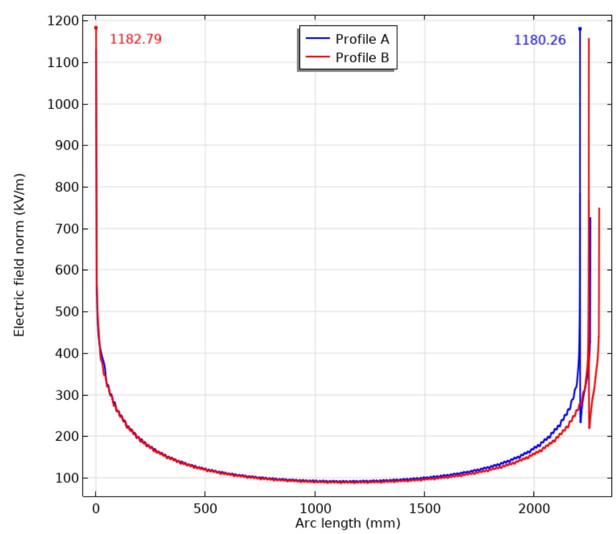

Figure 7: Electric Field Norm Along Arc Length of Insulator Profiles having 94mm defect length on LV side

For the defect at the ground side, this follows the HV side case with polarity reversed, the ground facing bottom edge collapses toward zero while the rod facing top edge is stressed (profile A: 859.45 kV/m; profile B: 841.91 kV/m), and the LV point reference value drops sharply (profile A: 619.10 to 387.32 kV/m, −37.4%; profile B: 644.82 to 399.41 kV/m,

−38.1%) while the HV side point stays near healthy. Unlike the HV side case, Profile A is here marginally more stressed than Profile B at the defect edge 859.45 vs 841.91 kV/m. As with the HV side case, the arc length plot figure 7 shows this as a sharp, single sided spike, now located near the grounded end of the curve, mirroring the HV side pattern but with reversed polarity along the profile.

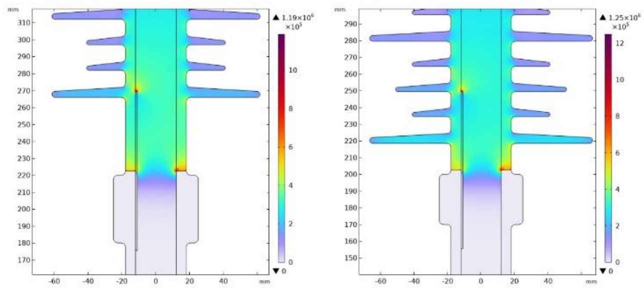

(a)

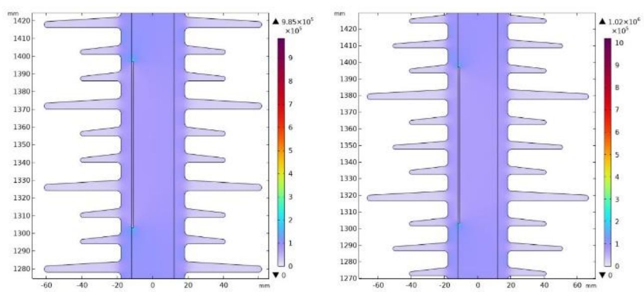

(b)

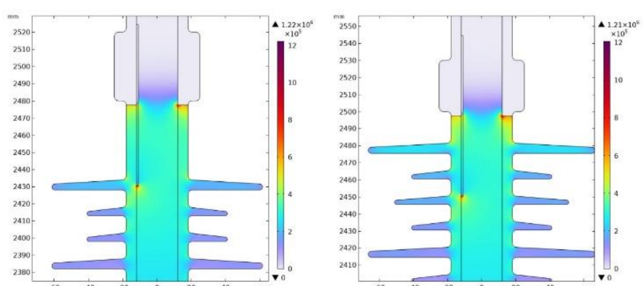

(c)

Figure 8: Electric Field surface plot of profile A and profile B having 94 mm defect length

3.3 Impact of Long 540 mm Length Internal Defect on Electric Field Distribution

For the defect at the HV side, as with the short defect, the electrode facing edge collapses toward zero while the reference point nearest the defect drops well below healthy (profile A: 638.74 to 455.15 kV/m, −28.7%; profile B: 663.41 to 471.50 kV/m, −28.9%), with the far LV point essentially unchanged. The rod facing top edge is stressed to 347.86 kV/m for profile A and 335.44 kV/m for profile B, Profile A marginally higher this time, a reversal from the short defect case as presented in table 5, and the surface plot of both the profiles are given in figure 11.

Table 5: Point Evaluation of Electric Field Norm on Insulator Profiles with 540 mm defect length.

Electric field norm (kV/m)				
Defect position	**Profile A**		**Profile B**	
	HV point	**LV point**	**HV point**	**LV point**
HV side	455.14	628.48	471.50	657.23
center	642.24	620.14	665.46	647.95
Ground side	644.47	444.49	677.57	459.86
Defect position	**Bottom edge of defect**	**Top edge of defect**	**Bottom edge of defect**	**Top edge of defect**
HV side	1.08E-04	347.85	0.0016	335.44
center	243.45	308.78	242.08	243.73
Ground side	341.40	1.03E-04	329.55	0.0016

The corresponding arc length plot figure 9 shows a broader, lower-amplitude spike than the 94 mm case at the same position, consistent with the longer defect distributing the same potential drop over a greater length rather than concentrating it at a sharp point.

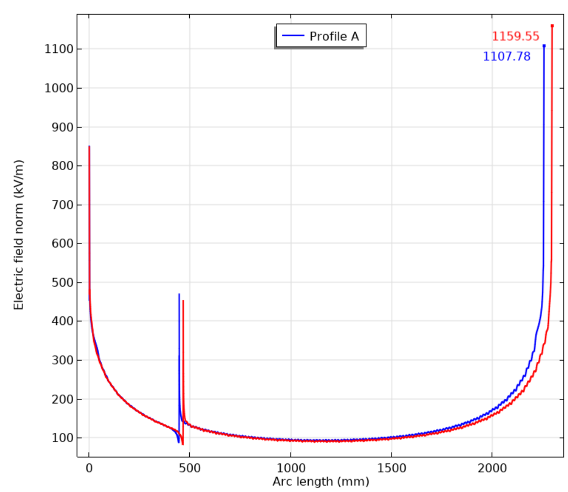

Figure 9: Electric Field Norm Along Arc Length of Insulator Profiles having 540 mm defect length on HV side

For the defect at the center, both reference points stay within ±0.6% of healthy, confirming the defect remains locally confined regardless of length. At the defect edges, the same profile dependent asymmetry pattern seen with the short defect reappears, Profile A's two edges differ by approx. 27% (243.45 and 308.78 kV/m), while Profile B's are nearly balanced (242.08 and 243.74 kV/m, <1%). This consistency across both defect lengths strengthens the earlier observation. Because the defect is long enough that its two edges are well separated along the rod, the arc length plot figure 10 shows two distinct, clearly separated spikes with a flat, reduced field plateau between them visually distinguishing the long floating defect from the single narrow double spike seen in the 94 mm center case.

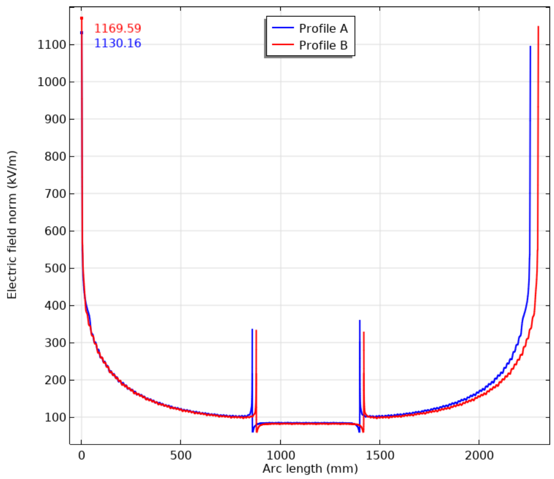

Figure 10: Electric Field Norm Along Arc Length of Insulator Profiles having 540 mm defect length at floating potential

For the defect at the ground side, this follows the HV side case, bottom edge value is approx. to 0, LV side point drops sharply (profile A: 619.10 to 444.49 kV/m, −28.2%; profile B: 644.82 to 459.87 kV/m, −28.7%), HV side point remains near to healthy condition values. Top facing rod edge stress: 341.41 kV/m (profile A) and 329.55 kV/m (profile B) again Profile A is at slightly higher stress. The arc length plot figure 11 again shows the broader, lower amplitude spike characteristic of the longer defect, located near the grounded end, mirroring the HV side long defect pattern.

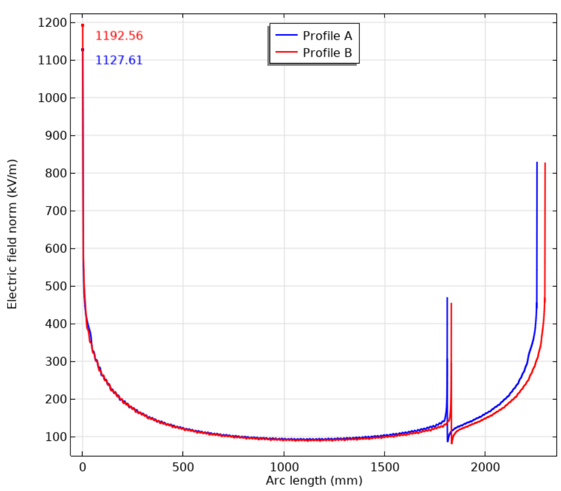

Figure 11: Electric Field Norm Along Arc Length of Insulator Profiles having 540 mm defect length on LV side

3.4 Discussion

The results establish a clear relationship between internal FRP rod defects and shed profile for insulators of the same voltage class. Defect position sets the underlying distortion pattern, electrode connected defects redistribute stress toward one

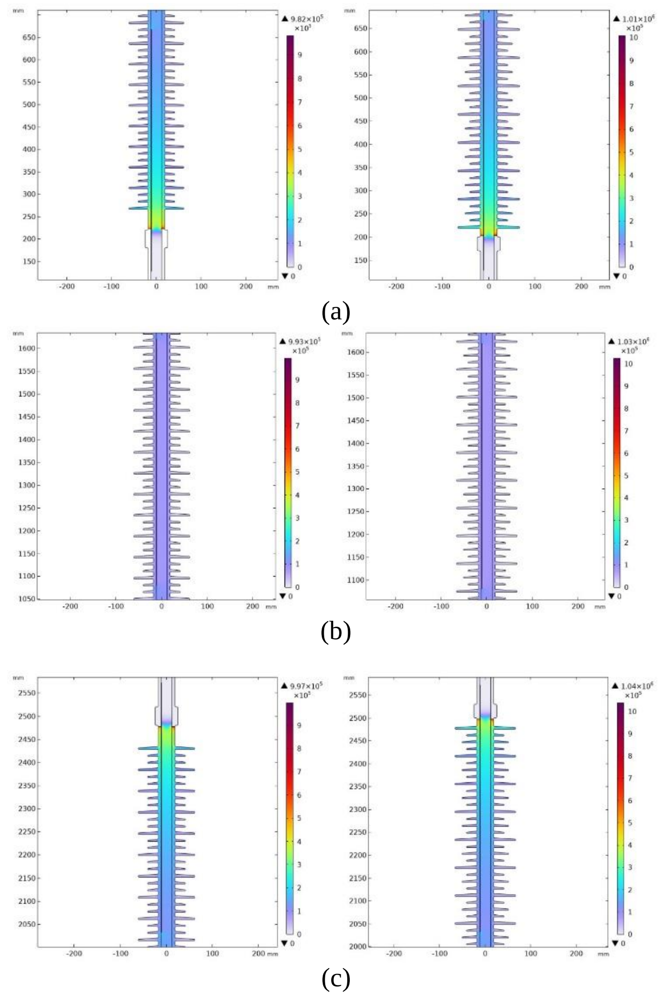

Figure 11: Electric Field surface plot of profile A and profile B having 540 mm defect length

edge and the nearest reference point, while floating center defects stress both edges symmetrically and this pattern holds identically in both profiles and defect length scales the severity of that pattern.

What varies systematically with shed profile is the magnitude and symmetry of the resulting stress, for an otherwise identical defect. At the HV side connected defect, Profile B consistently registers a higher field than Profile A (both defect lengths). At the center floating defect, Profile A consistently shows a pronounced edge-to-edge asymmetry that Profile B does not, again at both defect lengths. Since the two profiles are matched in overall length, core diameter, and end fittings, and differ only in shed geometry, this repeatable, position dependent divergence indicates that shed profile impacts the stress distribution in insulators, the same internal defect, at the same position, produces a measurably different field response depending on the surrounding shed geometry. This confirms that internal defect severity in composite insulators cannot be evaluated independent of shed profile, and profile specific defect behavior should be accounted for in insulator condition assessment and modeling.

4. CONCLUSION

This study aims to determine whether a relationship exists between internal FRP rod defects and shed profile for composite insulators of the same voltage class. A comparative 2D FEM analysis of two 400 kV profiles, differing only in shed geometry, under identical defect conditions (two lengths, three positions) shows that defect position and length govern the type and severity of field distortion consistently in both profiles, while shed profile systematically modulates the magnitude and symmetry of that distortion for an otherwise identical defect Profile B showing higher stress for HV side connected defects, and Profile A showing greater edge asymmetry for floating center defects, repeatably across both defect lengths. This demonstrates a measurable, position dependent interaction between internal defect behavior and external shed profile, indicating that profile geometry is a relevant parameter in assessing how internal defects manifest electrically, and not solely a surface pollution or creepage design consideration.

ACKNOWLEDGEMENT

The author sincerely acknowledges Electrical Engg. Department, FoTE**,** The Maharaja Sayajirao University of Vadodara, India for its continuous academic support and encouragement. The author also extends sincere thanks to the Electrical Research and Development Association (ERDA) Vadodara, India for its guidance which resulted in successful completion of this research paper.

REFERENCES

[1] C. V. Santoshbhai, A. S. Khopkar, and H. M. Patel, “Comprehensive Comparison of High Voltage Polymer and Porcelain Insulators in AC Systems,” *Engineering and Technology Journal*, vol. 11, no. 01, Jan. 2026, doi: 10.47191/etj/v11i01.38.

[2] C. V. Santoshbhai, A. S. Khopkar, and H. M. Patel, “A Study on Performance of Ageing High Voltage Polymer Insulators in AC Systems,” *Engineering and Technology Journal*, vol. 11, no. 07, Jul. 2026, doi: 10.47191/etj/v11i07.14.

[3] Y. Gao *et al*., "Comparative Investigation on Fracture of Suspension High Voltage Composite Insulators: A Review—Part I: Fracture Morphology Characteristics," in *IEEE Electrical Insulation Magazine*, vol. 37, no. 3, pp. 7-17, May/June 2021, doi: 10.1109/MEI.2021.9399912.

[4] G. Pang, Z. Zhang, J. Hu, Q. Hu, H. Zheng, and X. Jiang, “Analysis of Failures and Protective Measures for Core Rods in Composite Long-Rod Insulators of Transmission Lines,” Jun. 01, 2025, *Multidisciplinary Digital Publishing Institute (MDPI)*. doi: 10.3390/en18123138.

[5] Z. Yuan, Y. Tu, Y. Zhao, H. Jiang, and C. Wang, “Degradation behavior and aging mechanism of decay-like fractured GRP rod in composite insulator,” *IEEE Transactions on Dielectrics and Electrical Insulation*, vol. 26, no. 3, pp. 1027–1034, Jun. 2019, doi: 10.1109/tdei.2019.007788.

[6] C. Gao, Y. Peng, S. Zhang, B. Zhang, W. Li, and L. Li, “Mechanism Analysis of Composite Insulators Deterioration and Decay-Like Aging Caused by Internal Discharge in Transmission Lines,” *IEEE Access*, vol. 11, pp. 114582–114589, 2023, doi: 10.1109/ACCESS.2023.3321972.

[7] X. Li *et al.*, “A Study on the Influence of End-Sheath Aging and Moisture Absorption on Abnormal Heating of Composite Insulators,” *Coatings*, vol. 12, no. 7, Jul. 2022, doi: 10.3390/coatings12070898.

[8] G. Kone, C. Volat, and H. Ezzaidi, “Numerical investigation of electric field distortion induced by internal defects in composite insulators,” *High Voltage*, vol. 2, no. 4, pp. 253–260, Dec. 2017, doi: 10.1049/hve.2016.0096.

[9] G. Kone, C. Volat and H. Ezzaidi, "3D numerical investigation of internal defects in a 28 kV composite insulator," *2014 IEEE Electrical Insulation Conference (EIC)*, Philadelphia, PA, USA, 2014, pp. 208-212, doi: 10.1109/EIC.2014.6869377.

[10] M. Ramesh, L. Cui, and R. S. Gorur, “Impact of superficial and internal defects on electric field of composite insulators,” *International Journal of Electrical Power and Energy Systems*, vol. 106, pp. 327–334, Mar. 2019, doi: 10.1016/j.ijepes.2018.10.013.

[11] A. Phillips *et al.*, “Electric fields on AC composite transmission line insulators,” *IEEE Transactions on Power Delivery*, vol. 23, no. 2, pp. 823–830, 2008, doi: 10.1109/TPWRD.2007.911127.

[12] Z. Shen, L. Yuze, and Z. Bo, “Electric Fields Distribution of EHV AC Transmission Line Composite Insulators with Internal Conductive Defects,” in *2019 Asia Power and Energy Engineering Conference, APEEC 2019*, Institute of Electrical and Electronics Engineers Inc., May 2019, pp. 115–120. doi: 10.1109/APEEC.2019.8720704.

[13] J. Zhang, J. Shi, and J. Zhang, “Analysis of the Surface Electric Field Distribution of a 10 kV Faulty Composite Insulator,” *Electronics (Switzerland)*, vol. 11, no. 22, Nov. 2022, doi: 10.3390/electronics11223740.

[14] M. R. Halloum, B. S. Reddy, and G. N. Reddy, “Failure analysis of field-aged polymeric outdoor insulators and performance enhancement for electric stress using nonlinear field grading composites,” *Electrical Engineering*, vol. 106, no. 2, pp. 1147–1161, Apr. 2024, doi: 10.1007/s00202-023-01898-0.